Article

Formation of Carbon-Incorporated NiO@Co₃O₄ Nanostructures via a Direct Calcination Method and Their Application as Battery-Type Electrodes for Hybrid Supercapacitors

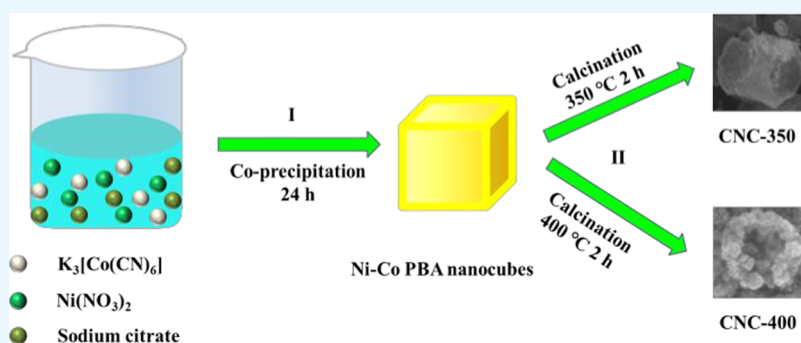Lichen Zhao, Huifang Zhang,* and Boxiang Ma

Read Online

ACCESS | Metrics & More | Article Recommendations

ABSTRACT: Nickel and cobalt oxides are promising electrode materials for supercapacitors, but their poor conductivity and sluggish kinetics seriously hinder their application. Herein, a simple one-step calcination method was proposed to prepare carbon-incorporated NiO@Co₃O₄ (denoted as CNC) using a NiCo Prussian blue analogue (NiCo-PBA) as a precursor. The effect of calcination temperature on the electrochemical behavior of CNC was investigated. Benefiting from the relatively large specific surface area and porous structure characteristics, when used as an electrode for supercapacitors, the CNC obtained at 400 °C shows the typical features of a battery-type electrode, with a good specific capacitance of 208.5 F g⁻¹ at 1 A g⁻¹ and a rate capability of 70.8% at 30 A g⁻¹. The hybrid supercapacitor (HSC) constructed with the optimum CNC electrode can provide a high energy density of 32.6 Wh kg⁻¹ at the corresponding power density of 750.0 W kg⁻¹ and an excellent cycling stability of 87.1% over 5000 cycles. This study provides a simple calcination method for preparing MOF-derived high-conductivity mixed metal oxide electrode materials for supercapacitors.

INTRODUCTION

Nowadays, the shortage of fossil fuel resources, environmental problems, and rapid economic growth have greatly increased the demand for sustainable and efficient energy storage technologies.[1−4] Among various energy storage devices, lithium-ion batteries (LIBs) and supercapacitors (SCs) have been extensively investigated.[5] LIBs have the advantages of high energy density and low self-discharge; however, their widespread application is hampered by long charging time, short cycle life, and low power density.[6−10] Compared with LIBs, supercapacitors (SCs) can provide high power density but have relatively low energy density.[11−14] Therefore, it is urgent to find energy storage devices with high energy and power density to fill the gap between LIBs and SCs.[15−17]

Hybrid supercapacitors (HSCs) have attracted growing attention due to their superior energy storage capability and power characteristics.[9,10] Commonly, a HSC is composed of a battery-type electrode as an energy source and a capacitor-type electrode as a power source, so it can combine the features of high specific capacitance of pseudocapacitors and high rate capability of electric double-layer supercapacitors (EDLCs).[18−20] Carbon-based materials (eg., activated carbon, graphene) are widely used as capacitor-type electrode materials, while transition metal compounds are usually used as battery-type electrode materials. Among various transition metal compounds, NiO and Co₃O₄ are two promising battery-type materials owing to their high theoretical specific capacitance and chemical stability.[21,22] However, the intrinsic poor electrical conductivity of NiO and Co₃O₄ leads to mismatch kinetics between NiO/Co₃O₄ and carbon-based materials, which greatly limits the performance of HSCs.[4,12,23]

To address this issue, numerous efforts have been made to develop NiO and/or Co_3O_4 electrode materials with improved electrical conductivity, such as preparing composite materials with graphene, carbon nanotubes, and other highly conductive materials,[24−28] preparing bimetallic materials,[29,30] directly growing on highly conductive support substrates,[31,32] atomic doping,[33,34] etc. Although great progress has been made in improving the conductivity, it is difficult to obtain two oxides simultaneously in these studies, and the synthesis methods are complex and poorly controllable; also, the interface formed between oxides and carbon materials will affect the electrochemical performance to a certain extent.

Herein, we designed carbon-incorporated $NiO@Co_3O_4$ nanostructures using NiCo-PBA as a precursor via a facile one-step calcination method. The synergistic effect of NiO and Co_3O_4 with high redox activity and the good conductivity provided by the carbon formed in situ endow the hybrid composite with excellent electrochemical performance as a battery-type material for SCs. The CNC electrode obtained at the optimum calcination temperature of 400 °C showed a specific capacitance of 208.5 F g^{-1} at 1 A g^{-1} and a rate capability of 70.8% when the current was increased 30 times. Moreover, a HSC based on the optimal CNC electrode was fabricated, which can deliver a high energy density of 32.6 Wh kg^{-1} at a power density of 750.0 W kg^{-1} and a long cycle life (87.1% over 5000 cycles). This work provides a facile method to prepare carbon-incorporated mixed metal oxides as effective electrodes for HSCs.

■ EXPERIMENTAL SECTION

Chemicals. All chemicals were analytical grade and were used as purchased without any treatment. $Ni(NO_3)_2 \cdot 6H_2O$ were purchased from Damao chemical reagent factory, and $C_6H_5Na_3O_7 \cdot 2H_2O$ and potassium hexacyanocobaltate (III) were purchased from Aladdin.

Synthesis of NiCo-PBA Nanocubes. NiCo-PBA nanocubes were synthesized by the following steps. First, $Ni(NO_3)_2 \cdot 6H_2O$ (0.696 g) was dissolved in 80 mL of deionized water, and then, 1.056 g of $C_6H_5Na_3O_7 \cdot 2H_2O$ was added to the solution with stirring. The above-mentioned solution was labeled as solution A. Second, 0.528 g of potassium hexacyanocobaltate (III) was dissolved in 80 mL of deionized water under magnetic stirring to form a homogeneous solution, labeled as solution B. Finally, solution B was poured into solution A, and the mixed solution was made to stand for 24 h to produce a blue-white precipitate. The precipitate was washed six times with deionized water and ethanol, collected by centrifugation, and dried in an oven.

Synthesis of CNC Nanostructures. CNC nanostructures were synthesized by a one-step calcination process of NiCo-PBA in air. The prepared NiCo-PBA precursor was placed in a porcelain boat and calcined in a tubular furnace at 350 °C (400, 450 °C) for 2 h, and the heating rate was maintained at 2 °C per minutes in the whole process. The obtained CNC products were denoted as CNC-350, CNC-400, and CNC-450.

Material Characterization. X-ray diffraction (XRD) was carried out on a Bruker D8 with Cu Kα radiation. An X-ray photoelectron spectrometer (XPS) was performed on a Thermo Scientific ESCALAB 250Xi. Scanning electron microscopy (SEM, ZEISS Sigma 300) and transmission electron microscopy (Tecnai G2 F20 S-Twin) were utilized to analyze the morphology of the products. The nitrogen

adsorption and desorption isotherms were obtained from JW-BK 122 W apparatus.

Electrochemical Tests. The working electrode was prepared by coating a slurry of CNC, polytetrafluoroethylene (PTFE), and acetylene black with a weight ratio of 80:10:10 on a nickel foam (area = 1 × 1 cm²). A standard three-electrode system with platinum as the counter electrode and Hg/HgO as the reference electrode was used to measure the electrochemical performances of CNC in 6 M KOH electrolyte. The mass loading for CNC-350 and CNC-400 was 2.6, 2.8, and 2.9 mg cm^{-2}. For the hybrid supercapacitor (HSC), the CNC electrode was used as a positive electrode with the activated carbon (AC) electrode as a negative electrode. The mass ratio of positive to negative electrode active materials was determined to be 1:0.41 by the charge balance.[35] All the electrochemical measurements were performed on a CHI 760E electrochemical working station (Chenhua). The specific capacitance (C, F g^{-1}) of CNC is calculated by eq 1

$$C = I\Delta t / m\Delta V \tag{1}$$

where I (A) represents the discharge current, $\triangle t$ (s) represents the discharge time, m (g) is the mass of active material, and $\triangle V$ (V) is the potential window.

The coulombic efficiency (η) of the hybrid electrode is calculated by eq 2.

$$\eta = \frac{t_d}{t_c} \tag{2}$$

where t_d (s) represents the discharge time and t_c(s) represents the charge time.

The specific capacitance (C, F g^{-1}), energy density (E, Wh kg^{-1}), and power density (P, W kg^{-1}) of the HSC device can be calculated by eqs 3−5.

$$C = I\Delta t / M\Delta V \tag{3}$$

$$E = \frac{1}{2}C\Delta V^2 \tag{4}$$

$$P = \frac{E}{\Delta t} \tag{5}$$

where I (A) is the discharge current, $\triangle t$ (s) is the discharge time, M (g) is the mass of active material of positive and negative electrodes of the device, and $\triangle V$ (V) is the potential window.

The b value was calculated by eq 6

$$i = a\nu^b \tag{6}$$

where i (A g^{-1}) is the sum of the capacitive and diffusion-controlled current, ν (mV s^{-1}) is the scan rate, and a and b are variables.

The contributions of the capacitive and diffusion-controlled current to the total storage charge are determined by eq 7

$$i = k_1\nu + k_2\nu^{1/2} \tag{7}$$

where $k_1\nu$ represents the capacitive current and $k_2\nu^{1/2}$ represents the diffusion-controlled current. The values of k_1 and k_2 can be obtained by plotting the curve between $i/\nu^{1/2}$ versus $\nu^{1/2}$.
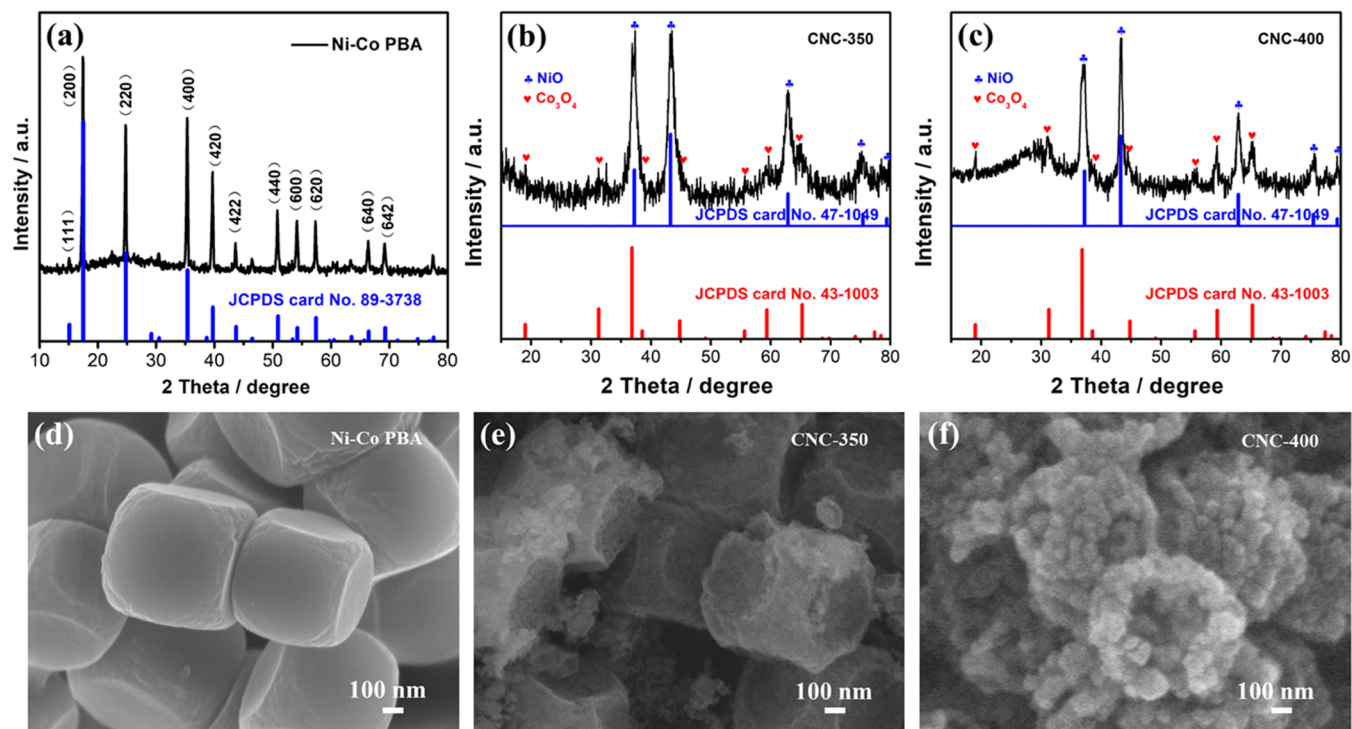
Figure 1. XRD patterns of (a) Ni-Co PBA, (b) CNC-350, and (c) CNC-400 and SEM images of (d) Ni-Co PBA, (e) CNC-350, and (f) CNC-400.
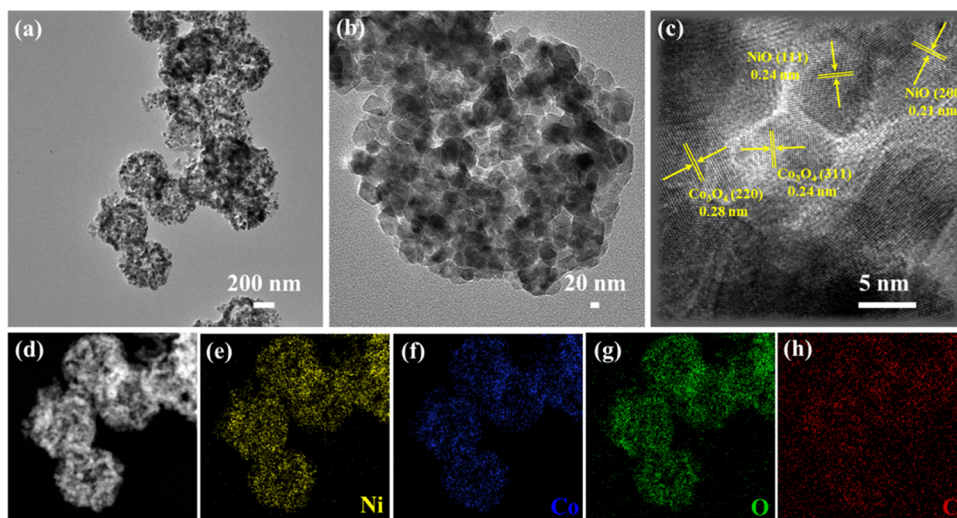

Figure 2. (a, b) TEM images and (c) HRTEM image of CNC-400, and (d−h) TEM image and the corresponding EDX mapping images of Ni, Co, O, and C, respectively.

■ RESULTS AND DISCUSSION

Figure 1a displays the XRD pattern of the precursor; all diffraction peaks are well matched with the $Ni_3[Co(CN)_6]_2$ phase (JCPDS card No. 89-3738), confirming the formation of Ni-Co PBA. After low-temperature calcination at 350 and 400 °C, $Ni_3[Co(CN)_6]_2$ can be completely converted into NiO and Co_3O_4, as revealed by the XRD pattern in Figure 1b,c; most of the diffraction peaks could be attributed to NiO (JCPDS card No. 47-1049) and Co_3O_4 (JCPDS card No. 43-1003). SEM was carried out to monitor the morphology of the Ni-Co PBA and CNC samples. As can be seen in Figure 1d, Ni-Co PBA shows a uniform cube shape with a size of about 500 nm and a smooth surface. The CNC product obtained at 350 °C maintains the original cube shape of Ni-Co PBA,

except for the six concave faces of the cubes (Figure 1e). After calcination at 400 °C, compared with Ni-Co PBA, the surface of the obtained CNC became rough and the edges of the cube became indistinct (Figure 1f). In addition, the CNC nanocubes are constructed by many small nanoparticles, which indicate that the CNC-400 product has a porous structure.

The TEM image in Figure 2a further confirms the porous structure of CNC-400. The high-magnification TEM image (Figure 2b) clearly reveals numerous small nanoparticles in the particles. The porous architecture is conducive to the excellent electrochemical performance of CNC, which can provide more contact area between the electrode and electrolyte and effectively shorten the ion transport distance during the
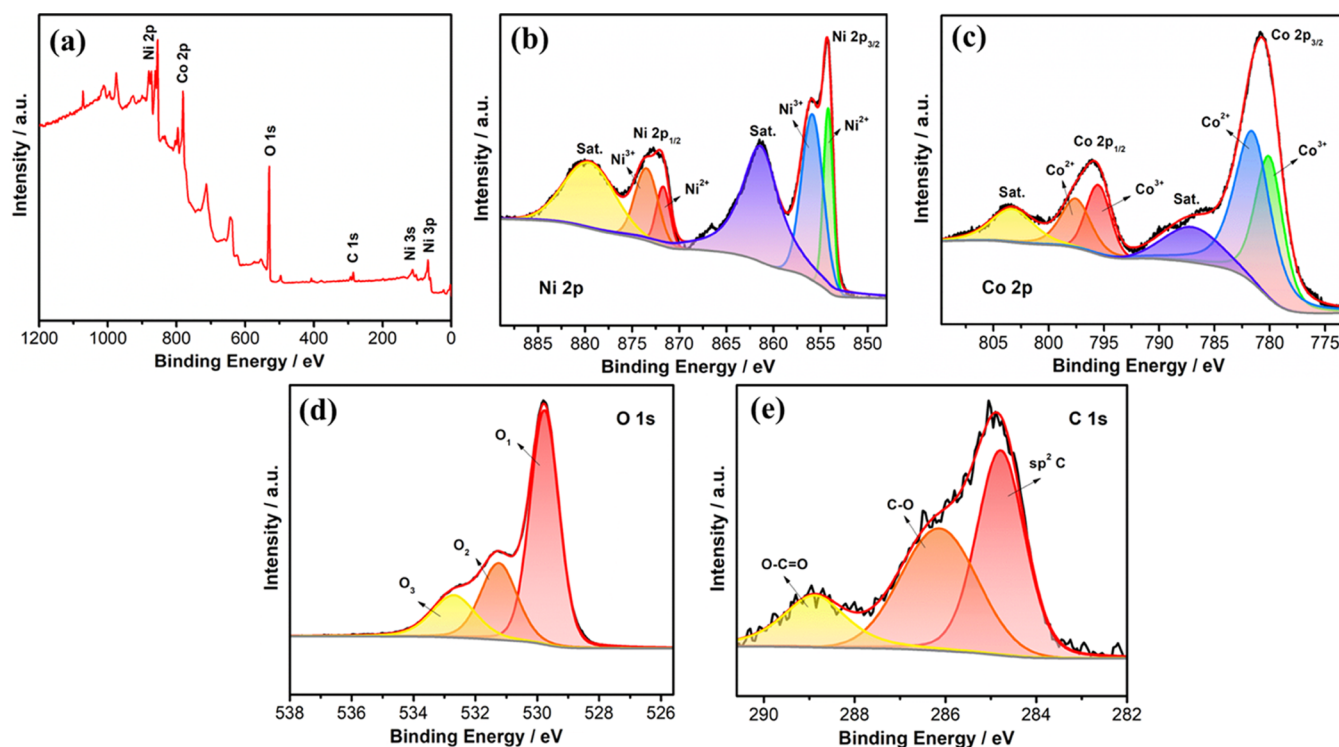
Figure 3. (a) XPS spectra of CNC and the magnified XPS spectra of (b) Ni 2p, (c) Co 2p, (d) O 1s, and (e) C 1s.
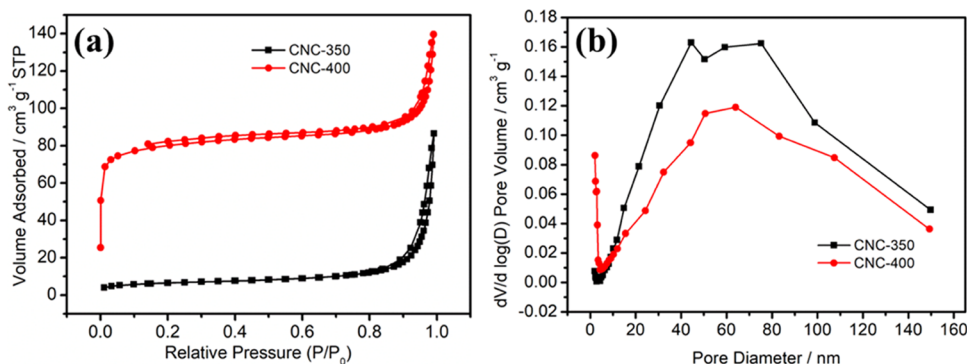

Figure 4. (a) Nitrogen adsorption−desorption isotherm and (b) corresponding pore size distribution curves of CNC-350 and CNC-400.

electrochemical reactions. Figure 2c shows the HRTEM image of CNC-400, with the lattice spacing of 0.21 and 0.24 nm corresponding to the (200) and (111) planes of NiO and lattice spacing of 0.24 and 0.28 nm corresponding to the (311) and (220) planes of Co_3O_4, respectively. Elemental mapping images in Figure 2d−h reveal that the Ni, Co, O, and C elements are homogeneously distributed throughout the sample.

The surface elements and chemical bond states of CNC were determined using XPS measurements. From the XPS full spectrum in Figure 3a, it was confirmed that Ni, Co, O, and C elements were contained in the CNC hybrids. From the Ni 2p, Co 2p, O 1s, and C 1s high-resolution spectra, the oxidation states of the elements were obtained. As shown in Figure 3b, Ni 2p spectra of CNC hybrids are deconvoluted into two doublets; the peaks located at 871.7 and 854.2 eV belong to Ni^{2+} in the standard Ni−O octahedral bonding configuration in cubic NiO, and the peaks located at 873.5 and 855.9 eV belong to the vacancy-induced Ni^{3+}. The satellite peaks at 879.5 and 861.4 eV can be attributed to Ni $2p_{1/2}$ and Ni $2p_{3/2}$,

respectively. These fitting peaks of Ni 2p demonstrate the existence of NiO.[36] In the Co 2p spectrum (Figure 3c), two peaks at 797.6 and 781.5 eV can be assigned to Co^{2+} and two peaks at 795.5 and 780.0 eV can be assigned to Co^{3+}. Additionally two shake-up satellite peaks at 803.3 and 787.0 eV were observed, which are a characteristic of spinel Co_3O_4. Figure 3d shows the high-resolution XPS spectrum of O 1s, which contains three oxygen contributions at 529.8 (O_1), 531.2 (O_2), and 532.7 eV (O_3). The O_1 component is assigned to lattice oxygen in the NiO and Co_3O_4 phases, the O_2 component is attributed to the defective oxygen in the oxide, and the O_3 component is attributed to the hydroxyl group on the hybrid surface.[37] The existence of oxygen defects can effectively regulate the electronic structure and improve the electrochemical performance of the oxide. As shown in Figure 3e, the C 1s XPS spectrum of the hybrid displays three peaks centered at 288.9, 286.1, and 284.8 eV, which can be assigned to the contributions from O−C=O, C−O bond, and graphite-like sp^2 C, respectively. The above-mentioned results of XPS
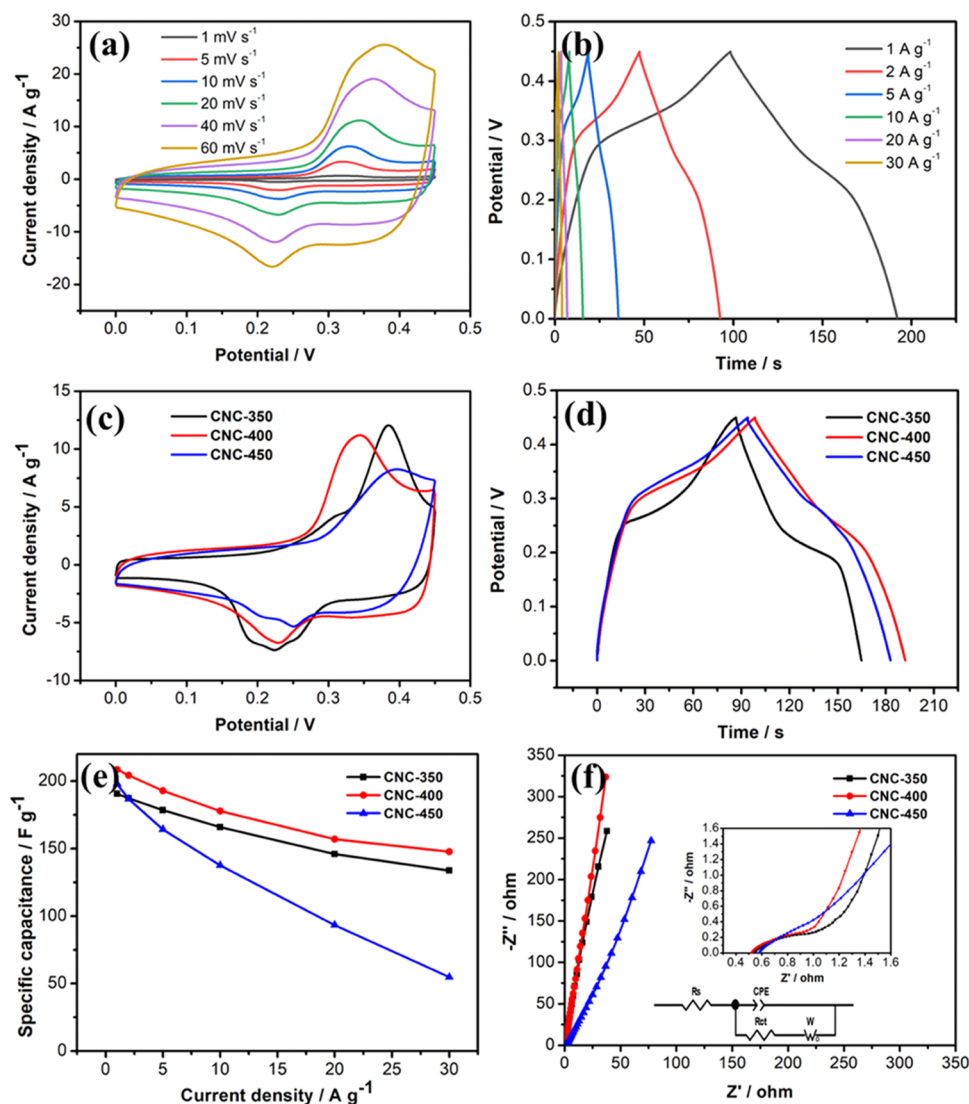
Figure 5. (a) CV profiles of the CNC-400 electrode at various scan rates; (b) GCD profiles of the CNC-400 electrode at various current densities; comparison of the electrochemical performances of CNC-350, CNC-400, and CNC-450 electrodes, (c) CV profiles at 20 mV s^{-1}, (d) GCD profiles at 1 A g^{-1}, (e) specific capacitance at various current densities; and (f) Nyquist plots; the inset is an equivalent circuit model.

indicate that the synthesized product is a carbon-incorporated NiO@Co$_3$O$_4$ hybrid.

The specific surface area and porosity of CNC-350 and CNC-400 were investigated by a nitrogen adsorption–desorption isotherm based on the Brunauer–Emmett–Teller (BET) method and Barrett–Joyner–Halenda (BJH) model. As shown in Figure 4a, compared with CNC-350, the isotherms of CNC-400 increased dramatically at P/P_0 <0.001, indicating the existence of micropores. In addition, the steep rise isotherm at P/P_0 > 0.9 verified the existence of micropores and macropores. Ascribed to the porous structural features, the BET specific surface area of CNC-400 is 258.5 m^2 g^{-1}, which is much larger than that of CNC-350 (21.8 m^2 g^{-1}). Figure 4b shows that CNC-400 has significantly increased micropores than those of CNC-350. Enough micropores can bring a large surface area, leading to a more accessible pathway for electrochemical reactions. Moreover, great quantities of micropores and macropores are located between 5 and 140 nm, which can provide a low-ion transfer resistance path and reduce the ion diffusion distance to the inner surface during the rapid charge–discharge process. Such a hierarchical porous

characteristic is beneficial to promote the electrochemical activity of CNC-400 in the process of energy storage.

To quantify the energy storage performance of CNC, the electrochemical behavior of CNC obtained at a series of calcination temperatures (350, 400, and 450 °C) was investigated. Figure 5a shows the cyclic voltammetry (CV) profiles of the CNC-400 electrode at different scan rates of 1–60 mV s^{-1}. A pair of redox peaks originating from the Ni^{2+}/Ni^{3+} and Co^{2+}/Co^{3+} are observed, indicating the typical Faraday characteristic. In addition, the potential difference between redox peaks increases with the increase of the scanning rate, indicating that the Faradaic behavior is quasi-reversible. As shown in Figure 5b, an obvious charge and discharge plateau can be observed in the galvanostatic charge/discharge (GCD) profile of the CNC-400 electrode, which further confirms the battery-type behaviors. Figure 5c shows the CV curves of CNC-350, CNC-400, and CNC-450 electrodes at 20 mV s^{-1}. Obviously, compared with CNC-350 and CNC-450 electrodes, the CNC-400 electrode shows a larger integral CV area, which means a larger capacitive performance. As shown in Figure 5d, the large capacitance of
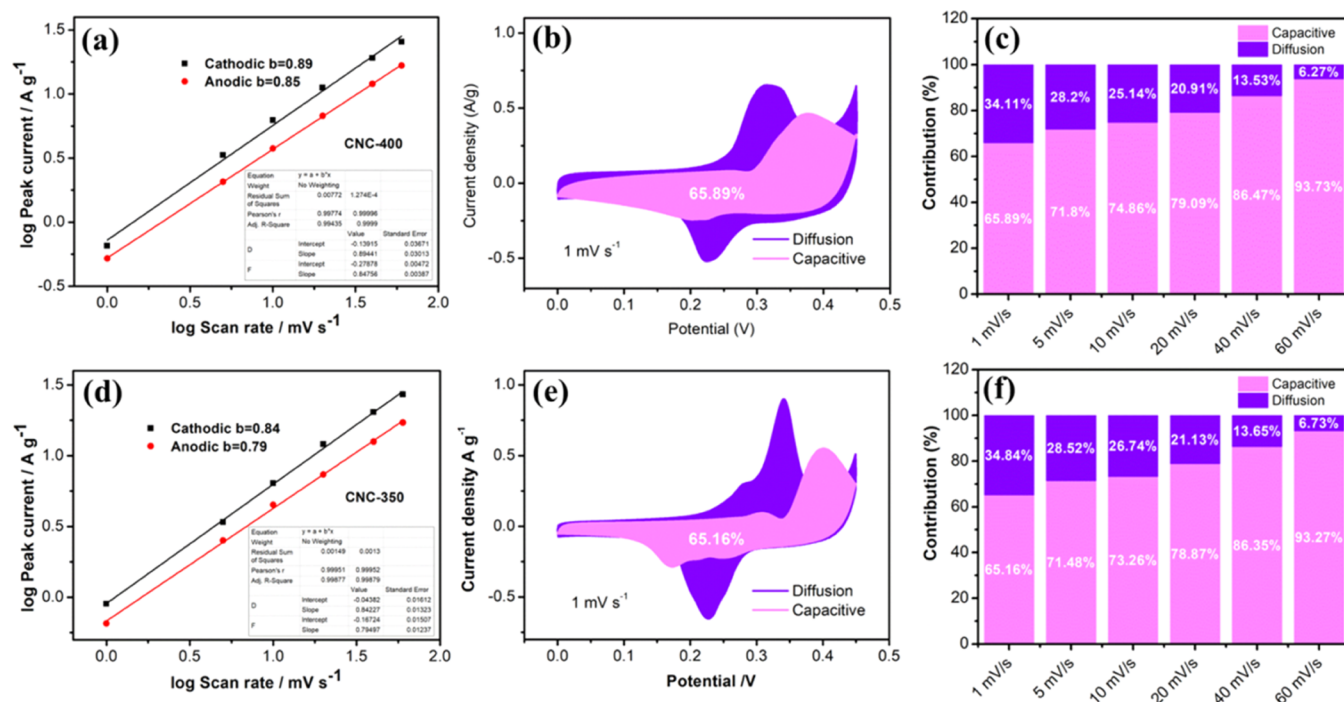
Figure 6. log (ν) versus log(i) for (a) CNC-400 and (d) CNC-350; the capacitive and diffusion-controlled current contribution in the total current at 1 mV s^{-1} for (b) CNC-400 and (e) CNC-350; and the capacitive and diffusion-controlled contributions at different scan rates for (c) CNC-400 and (f) CNC-350.

the CNC-400 electrode was verified by the longer discharge time in the GCD curve. In detail, the specific capacitances of the three CNC electrodes were calculated and are presented in Figure 5e. It can be clearly seen that the CNC-400 electrode exhibits improved capacitance compared to that of CNC-350 and CNC-450 electrodes at all tested current densities. For the CNC-400 electrode, the specific capacitance can reach 208.5 F g^{-1} at 1 A g^{-1} and retain a good rate capability of 70.8% at 30 A g^{-1}.

The electrochemical impedance spectroscopy (EIS) curves of the three CNC electrodes are shown in Figure 5f, which consist of both a straight line in the low-frequency region and a semicircle in the high-frequency region. From the equivalent circuit model (inset in Figure 5f), the equivalent series resistance (R_s) and charge transfer resistance (R_{ct}) of the CNC-400 electrode are 0.54 and 0.25 Ω, respectively, indicating a high electrical conductivity and a fast ion/electron transfer rates. The small R_s and R_{ct} can be attributed to the improved conductivity provided by the introduction of carbon into the hybrid material. Compared with the CNC-400 electrode, the R_s and R_{ct} values of the CNC-350 electrode are almost the same as those of the CNC-400 electrode, while the CNC-450 electrode has larger R_s and R_{ct} values. Additionally, the CNC-400 electrode exhibits a lower ion diffusion resistance (W) compared with that of CNC-350 and CNC-450 electrodes, which means faster ion mobility. These features indicate that CNC-400 could be a suitable electrode material with excellent performance for SCs.

The electrochemical kinetic behaviors of CNC-350 and CNC-400 electrodes were further compared and analyzed using the equation $i = a\nu^b$ and $i = \kappa_1\nu + \kappa_2\nu^{1/2}$. In the first equation, if the calculated b value is 0.5, the current response is diffusion-controlled and if the b value is 1.0, the current is surface-controlled.[2] Figure 6a shows that the cathodic and

anodic b values for CNC-400 are 0.89 and 0.85, respectively, and the b values for CNC-350 are 0.84 and 0.79 (Figure 6d), suggesting the synergistic effect of diffusion-controlled and capacitive behavior of the two electrodes. The low scan rate is conducive to the diffusion of more ions into the electrode; as shown in Figure 6b, even at a low scan rate of 1 mV s^{-1}, the capacitive proportion in the total charge storage can reach 65.89% for CNC-400, which is still larger than that of the diffusion-controlled process. In Figure 6c, it can be clearly seen that with the scanning rate increasing from 1 to 60 mV s^{-1}, the contributions of the capacitive current to the total charge storage for CNC-400 increase from 65.89 to 93.73%. For CNC-350, at 1 mV s^{-1}, the capacitive proportion in the total charge storage is 65.16% (Figure 6e). As the scanning rate increases from 1 to 60 mV s^{-1}, the capacitive contributions increase from 65.16 to 93.27% (Figure 6f). In comparison with CNC-350, the CNC-400 electrode shows a higher level of capacitive contribution, which is beneficial for rapid ion and electron transfer.[38]

To further evaluate the practicability of CNC, a HSC device was fabricated using CNC-400 as a positive electrode and AC as a negative electrode, with a piece of polypropylene paper as a separator and 6 M KOH as an electrolyte. (Figure 7a). In this HSC, the battery-type CNC electrode was used as the energy source with the capacitor-type AC electrode as the power source, which can provide both high energy and power density. As shown in Figure 7b, the AC electrode performs well in a potential window of −1.0−0 V and the CNC-400 electrode operates well in a potential window of 0−0.45 V. Based on this, we tested the HSC device in different potential windows and found that the optimal potential window for the device is 1.5 V (Figure 7c). CV profiles of the HSC device at scan rates in the range of 1−60 mV s^{-1} show that the current is contributed by the electric double-layer capacitance and pseudocapacitance
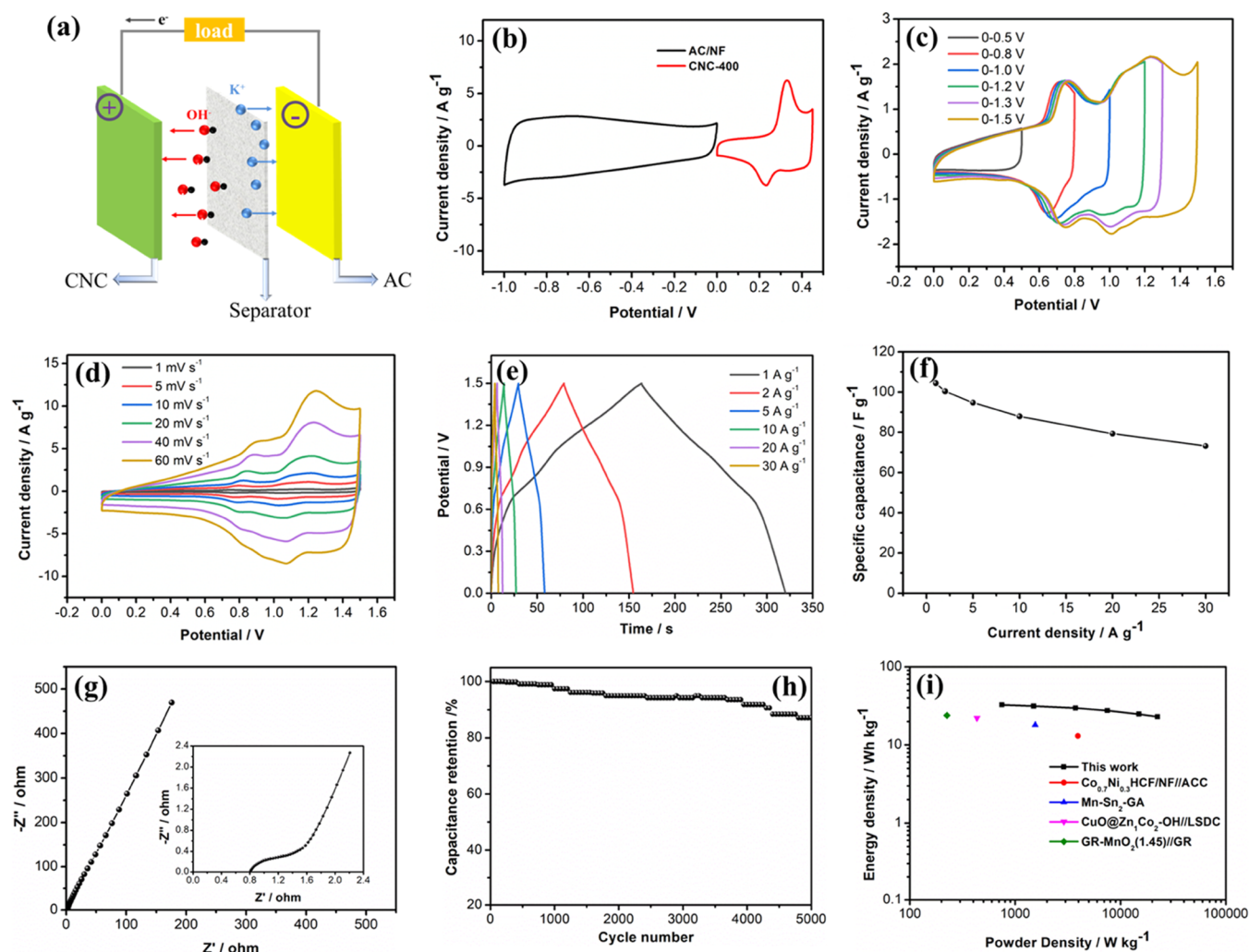
Figure 7. (a) Schematic illustration of the HSC device with CNC and AC as positive and negative electrodes, respectively; (b) CV profile of CNC and AC electrodes at 10 mV s^{-1}; the electrochemical performance of the device; (c) CV profiles collected at 0.5 V to 1.5 V at 10 mV s^{-1}; (d) CV profiles at various scan rates, (e) GCD profiles at various current densities; (f) specific capacitance at various current densities; (g) EIS curve; (h) cycling stability at 6 A g^{-1}; and (i) Ragone plot.

(Figure 7d). The CV shape was maintained well with increasing scan rate, demonstrating the high reversibility and excellent capacitive performance of the device.[39,40] Figure 7e shows that the GCD curves were almost symmetrical, indicating the stable charge storage of the HSC device.[3] The HSC device delivers a high specific capacitance of 104.4 F g^{-1} at 1 A g^{-1} and retained 73.2 F g^{-1} at 30 A g^{-1}, which suggest a good rate capability (Figure 7f). As seen in the EIS plot in Figure 7g, a small R_s and R_{ct} were observed, indicating the low internal resistance and low charge transfer resistance of the HSC device. The cycling stability was also investigated at 6 A g^{-1} over 5000 cycles; as illustrated in Figure 7h, the specific capacitance decreased to 87.1% of the initial capacitance obtained in the first cycle. Energy density and power density were calculated based on eqs 4 and 5; as shown in Figure 7i, a maximum energy density of 32.6 Wh kg^{-1} at the corresponding power density of 750.0 W kg^{-1} was observed, which is superior or comparable to those of the previous studies, such as Co$_{0.7}$Ni$_{0.3}$HCF/NF//ACC,[41] Mn-SnS$_2$-GA,[42] CuO@Zn$_1$Co$_2$-OH//LSDC,[43] GR-MnO$_2$(1.45)//GR,[44] and so on. The outstanding performance of the HSC device demonstrates

that the carbon-incorporated NiO@Co$_3$O$_4$ hybrid material is suitable for potential applications in the field of energy storage.

■ CONCLUSIONS

In summary, a carbon-incorporated NiO@Co$_3$O$_4$ hybrid was successfully synthesized from the NiCo-PBA precursor via a simple one-step calcination method. The novel composite combines the advantages of NiO, Co$_3$O$_4$, and C and can be utilized as an effective electrode for the HSC. The CNC obtained at 400 °C exhibited a better electrochemical performance than that of the CNC obtained at 350 and 450 °C, which can deliver a specific capacitance of 208.5 F g^{-1} at 1 A g^{-1} and a good rate performance of 70.8%. Furthermore, the assembled HSC device can deliver a high energy density of 32.6 Wh kg^{-1} at a power density of 750.0 W kg^{-1} and an excellent cycle life of 87.1% after 5000 cycles. This work provides a facile synthesis method for the preparation of carbon-incorporated mixed metal oxides, which can be used as functional material for energy storage.

■ AUTHOR INFORMATION

Corresponding Author

Huifang Zhang − *College of Mechatronics Engineering, North University of China, Taiyuan 030051, P. R. China;* ⊙ orcid.org/0000-0001-6920-4069; Email: hfzhang@nuc.edu.cn

Authors

Lichen Zhao − *School of Engineering and Computer Science, Oakland University, Michigan 48309, United States*

Boxiang Ma − *College of Mechatronics Engineering, North University of China, Taiyuan 030051, P. R. China*

Complete contact information is available at:
https://pubs.acs.org/10.1021/acsomega.3c00254

Notes

The authors declare no competing financial interest.

■ REFERENCES

(1) Zuo, W.; Li, R.; Zhou, C.; Li, Y.; Xia, J.; Liu, J. Battery-Supercapacitor Hybrid Devices: Recent Progress and Future Prospects. *Adv. Sci.* **2017**, *4*, No. 1600539.

(2) Wei, F.; Wei, Y.; Wang, J.; Han, M.; Lv, Y. N, P dual doped foamy-like carbons with abundant defect sites for zinc ion hybrid capacitors. *Chem. Eng. J.* **2022**, *450*, No. 137919.

(3) Zhao, K.; Sun, X.; Wang, Z.; Huang, C.; Li, D.; Liu, J. Sheet-like NiCo-layered double hydroxide anchored on N self-doped hierarchical porous carbon aerogel from chitosan for high-performance supercapacitors. *J. Alloys Compd.* **2022**, *921*, No. 166036.

(4) Liang, Z.; Qu, C.; Zhou, W.; Zhao, R.; Zhang, H.; Zhu, B.; Guo, W.; Meng, W.; Wu, Y.; Aftab, W.; Wang, Q.; Zou, R. Synergistic Effect of Co-Ni Hybrid Phosphide Nanocages for Ultrahigh Capacity Fast Energy Storage. *Adv. Sci.* **2019**, *6*, No. 1802005.

(5) Xiang, G.; Meng, Y.; Qu, G.; Yin, J.; Teng, B.; Wei, Q.; Xu, X. Dual-functional NiCo$_2$S$_4$ polyhedral architecture with superior electrochemical performance for supercapacitors and lithium-ion batteries. *Sci. Bull.* **2020**, *65*, 443−451.

(6) Cai, L.; Zhang, Q.; Mwizerwa, J. P.; Wan, H.; Yang, X.; Xu, X.; Yao, X. Highly Crystalline Layered VS$_2$ Nanosheets for All-Solid-State Lithium Batteries with Enhanced Electrochemical Performances. *ACS Appl. Mater. Interfaces* **2018**, *10*, 10053−10063.

(7) Shao, J.; Wan, Z.; Liu, H.; Zheng, H.; Gao, T.; Shen, M.; Qu, Q.; Zheng, H. Metal organic frameworks-derived Co$_3$O$_4$ hollow dodecahedrons with controllable interiors as outstanding anodes for Li storage. *J. Mater. Chem. A* **2014**, *2*, 12194−12200.

(8) Chen, P.; Zhou, W.; Xiao, Z.; Li, S.; Chen, H.; Wang, Y.; Wang, Z.; Xi, W.; Xia, X.; Xie, S. In situ anchoring MnO nanoparticles on self-supported 3D interconnected graphene scroll framework: A fast kinetics boosted ultrahigh-rate anode for Li-ion capacitor. *Energy Storage Mater.* **2020**, *33*, 298−308.

(9) Wang, Q.; Wen, Z. H.; Li, J. H. A Hybrid Supercapacitor Fabricated with a Carbon Nanotube Cathode and a TiO$_2$−B Nanowire Anode. *Adv. Funct. Mater.* **2006**, *16*, 2141−2146.

(10) Lee, S. W.; Yabuuchi, N.; Gallant, B. M.; Chen, S.; Kim, B. S.; Hammond, P. T.; Shao-Horn, Y. High-power lithium batteries from functionalized carbon-nanotube electrodes. *Nat. Nanotechnol.* **2010**, *5*, 531−537.

(11) Wan, L.; Wang, Y.; Zhang, Y.; Du, C.; Chen, J.; Xie, M.; Tian, Z.; Zhang, W. Designing FeCoP@NiCoP heterostructured nanosheets with superior electrochemical performance for hybrid supercapacitors. *J. Power Sources* **2021**, *506*, No. 230096.

(12) Qu, C.; Liang, Z.; Jiao, Y.; Zhao, B.; Zhu, B.; Dang, D.; Dai, S.; Chen, Y.; Zou, R.; Liu, M. ″One-for-All″ Strategy in Fast Energy Storage: Production of Pillared MOF Nanorod-Templated Positive/Negative Electrodes for the Application of High-Performance Hybrid Supercapacitor. *Small* **2018**, *14*, No. 1800285.

(13) Barai, H. R.; Lopa, N. S.; Ahmed, F.; Khan, N. A.; Ansari, S. A.; Joo, S. W.; Rahman, M. M. Synthesis of Cu-Doped Mn$_3$O$_4$@Mn-Doped CuO Nanostructured Electrode Materials by a Solution Process for High-Performance Electrochemical Pseudocapacitors. *ACS Omega* **2020**, *5*, 22356−22366.

(14) Taslim, R.; Apriwandi, A.; Taer, E. Novel Moringa oleifera Leaves 3D Porous Carbon-Based Electrode Material as a High-Performance EDLC Supercapacitor. *ACS Omega* **2022**, *7*, 36489−36502.

(15) Hai, Y.; Tao, K.; Dan, H.; Liu, L.; Gong, Y. Cr-doped (Co, Ni)$_3$S$_4$/Co$_9$S$_8$/Ni$_3$S$_2$ nanowires/nanoparticles grown on Ni foam for hybrid supercapacitor. *J. Alloys Compd.* **2020**, *835*, No. 155254.

(16) Zhai, R.; Xiao, Y.; Ding, T.; Wu, Y.; Chen, S.; Wei, W. Construction of NiCo$_2$S$_4$ heterostructure based on electrochemically exfoliated graphene for high-performance hybrid supercapacitor electrode. *J. Alloys Compd.* **2020**, *845*, No. 156164.

(17) Matheswaran, P.; Karuppiah, P.; Chen, S. M.; Thangavelu, P.; Ganapathi, B. Fabrication of g-C$_3$N$_4$ Nanomesh-Anchored Amorphous NiCoP$_2$O$_7$: Tuned Cycling Life and the Dynamic Behavior of a Hybrid Capacitor. *ACS Omega* **2018**, *3*, 18694−18704.

(18) Zhao, B.; Zhang, L.; Zhang, Q.; Chen, D.; Cheng, Y.; Deng, X.; Chen, Y.; Murphy, R.; Xiong, X.; Song, B.; Wong, C. P.; Wang, M. S.; Liu, M. Rational Design of Nickel Hydroxide-Based Nanocrystals on Graphene for Ultrafast Energy Storage. *Adv. Energy Mater.* **2017**, *8*, No. 1702247.

(19) Dubal, D. P.; Ayyad, O.; Ruiz, V.; Gomez-Romero, P. Hybrid energy storage: the merging of battery and supercapacitor chemistries. *Chem. Soc. Rev.* **2015**, *44*, 1777−1790.

(20) Shimamura, N.; Kanda, R.; Matsukubo, Y.; Hirai, Y.; Abe, H.; Hirai, Y.; Yoshida, T.; Yabu, H.; Masuhara, A. Preparation of Hierarchic Porous Films of alpha-MnO$_2$ Nanoparticles by Using the Breath Figure Technique and Application for Hybrid Capacitor Electrodes. *ACS Omega* **2019**, *4*, 3827−3831.

(21) Meng, T.; Xu, Q.-Q.; Wang, Z.-H.; Li, Y.-T.; Gao, Z.-M.; Xing, X.-Y.; Ren, T.-Z. Co$_3$O$_4$ Nanorods with Self-assembled Nanoparticles in Queue for Supercapacitor. *Electrochim. Acta* **2015**, *180*, 104−111.

(22) Yan, Y.; Ding, S.; Zhou, X.; Hu, Q.; Feng, Y.; Zheng, Q.; Lin, D.; Wei, X. Controllable preparation of core-shell Co$_3$O$_4$@CoNiS nanowires for ultra-long life asymmetric supercapacitors. *J. Alloys Compd.* **2021**, *867*, No. 158941.

(23) Wang, D.-G.; Liang, Z.; Gao, S.; Qu, C.; Zou, R. Metal-organic framework-based materials for hybrid supercapacitor application. *Coord. Chem. Rev.* **2020**, *404*, No. 213093.

(24) Wang, L.; Zheng, Y.; Wang, X.; Chen, S.; Xu, F.; Zuo, L.; Wu, J.; Sun, L.; Li, Z.; Hou, H.; Song, Y. Nitrogen-doped porous carbon/Co$_3$O$_4$ nanocomposites as anode materials for lithium-ion batteries. *ACS Appl. Mater. Interfaces* **2014**, *6*, 7117−7125.

(25) Guan, Q.; Cheng, J.; Wang, B.; Ni, W.; Gu, G.; Li, X.; Huang, L.; Yang, G.; Nie, F. Needle-like Co$_3$O$_4$ anchored on the graphene with enhanced electrochemical performance for aqueous supercapacitors. *ACS Appl. Mater. Interfaces* **2014**, *6*, 7626−7632.

(26) Zallouz, S.; Réty, B.; Vidal, L.; Le Meins, J.-M.; Matei Ghimbeu, C. Co$_3$O$_4$ Nanoparticles Embedded in Mesoporous Carbon for Supercapacitor Applications. *ACS Appl. Nano Mater.* **2021**, *4*, 5022−5037.

(27) Zhu, J.; Tu, W.; Pan, H.; Zhang, H.; Liu, B.; Cheng, Y.; Deng, Z.; Zhang, H. Self-Templating Synthesis of Hollow Co$_3$O$_4$ Nanoparticles Embedded in N,S-Dual-Doped Reduced Graphene Oxide for Lithium Ion Batteries. *ACS Nano* **2020**, *14*, 5780−5787.

(28) Wang, X.; Li, M.; Chang, Z.; Wang, Y.; Chen, B.; Zhang, L.; Wu, Y. Orientated Co$_3$O$_4$ Nanocrystals on MWCNTs as Superior Battery-Type Positive Electrode Material for a Hybrid Capacitor. *J. Electrochem. Soc.* **2015**, *162*, A1966−A1971.

(29) Du, J.; Zhou, G.; Zhang, H.; Cheng, C.; Ma, J.; Wei, W.; Chen, L.; Wang, T. Ultrathin Porous NiCo$_2$O$_4$ Nanosheet Arrays on Flexible Carbon Fabric for High-Performance Supercapacitors. *ACS Appl. Mater. Interfaces* **2013**, *5*, 7405−7409.

(30) Zheng, J.; Peng, X.; Xu, Z.; Gong, J.; Wang, Z. Cationic Defect Engineering in Spinel NiCo$_2$O$_4$ for Enhanced Electrocatalytic Oxygen Evolution. *ACS Catal.* **2022**, *12*, 10245−10254.

(31) Liu, Q.; Lu, C.; Li, Y. Controllable synthesis of ultrathin nickel oxide sheets on carbon cloth for high-performance supercapacitors. *RSC Adv.* **2017**, *7*, 23143−23148.

(32) Guo, C.; Zhang, Y.; Yin, M.; Shi, J.; Zhang, W.; Wang, X.; Wu, Y.; Ma, J.; Yuan, D.; Jia, C. Co$_3$O$_4$@Co$_3$S$_4$ core-shell neuroid network for high cycle-stability hybrid-supercapacitors. *J. Power Sources* **2021**, *485*, No. 229315.

(33) Han, X.; Wang, B.; Yang, C.; Meng, G.; Zhao, R.; Hu, Q.; Triana, O.; Iqbal, M.; Li, Y.; Han, A.; Liu, J. Inductive Effect in Mn-Doped NiO Nanosheet Arrays for Enhanced Capacitive and Highly Stable Hybrid Supercapacitor. *ACS Appl. Energy Mater.* **2019**, *2*, 2072−2079.

(34) Liu, X.; Xi, W.; Li, C.; Li, X.; Shi, J.; Shen, Y.; He, J.; Zhang, L.; Xie, L.; Sun, X.; Wang, P.; Luo, J.; Liu, L.-M.; Ding, Y. Nanoporous Zn-doped Co$_3$O$_4$ sheets with single-unit-cell-wide lateral surfaces for efficient oxygen evolution and water splitting. *Nano Energy* **2018**, *44*, 371−377.

(35) Li, Q.; Lu, C.; Xiao, D.; Zhang, H.; Chen, C.; Xie, L.; Liu, Y.; Yuan, S.; Kong, Q.; Zheng, K.; Yin, J. β-Ni(OH)$_2$ Nanosheet Arrays Grown on Biomass-Derived Hollow Carbon Microtubes for High-Performance Asymmetric Supercapacitors. *ChemElectroChem* **2018**, *5*, 1279−1287.

(36) Li, Z.; Zhao, J.; Nie, J.; Yao, S.; Wang, J.; Feng, X. Co$_3$O$_4$/NiO/C composites derived from zeolitic imidazolate frameworks (ZIFs) as high-performance anode materials for Li-ion batteries. *J. Solid State Electrochem.* **2020**, *24*, 1133−1142.

(37) Lü, Y.; Zhan, W.; He, Y.; Wang, Y.; Kong, X.; Kuang, Q.; Xie, Z.; Zheng, L. MOF-Templated Synthesis of Porous Co$_3$O$_4$ Concave Nanocubes with High Specific Surface Area and Their Gas Sensing Properties. *ACS Appl. Mater. Interfaces* **2014**, *6*, 4186−4195.

(38) Xu, H.; Liu, Y.; Qiang, T.; Qin, L.; Chen, J.; Zhang, P.; Zhang, Y.; Zhang, W.; Tian, W.; Sun, Z. Boosting sodium storage properties of titanium dioxide by a multiscale design based on MOF-derived strategy. *Energy Storage Mater.* **2019**, *17*, 126−135.

(39) Sui, Q.; Yu, Y.; Xiang, C.; Wang, Q.; Sun, L.; Xu, F.; Zhang, J.; Zou, Y. Static adsorption of MOFs nanosheets on 3D nanocubes for supercapacitor electrode materials. *J. Alloys Compd.* **2022**, *921*, No. 165982.

(40) Wang, M.-X.; Zeng, H.-Y.; Zhang, K.; Long, Y.-W.; Xu, S.; Yan, W. Enhanced supercapacitor performance of ultrathin NiCoMn(OH) nanosheets over NiCo$_2$O$_4$ nanoarray on Ni foam. *J. Alloys Compd.* **2022**, *921*, No. 165976.

(41) Chandra Reddy Niragatti, S.; Thupakula Venkata Madhukar, S.; Kim, J.; Yoo, K. In-situ-grown Co-doped Ni-hexacyanoferrate/Ni-foam composites as battery-type electrode materials for aqueous hybrid supercapacitors. *J. Alloys Compd.* **2022**, *918*, No. 165638.

(42) Chu, H.; Zhang, F.; Pei, L.; Cui, Z.; Shen, J.; Ye, M. Ni, Co and Mn doped SnS$_2$-graphene aerogels for supercapacitors. *J. Alloys Compd.* **2018**, *767*, 583−591.

(43) Liu, G.; Song, X.-Z.; Zhang, S.; Chen, X.; Liu, S.; Meng, Y.; Tan, Z. Hierarchical CuO@ZnCo−OH core-shell heterostructure on copper foam as three-dimensional binder-free electrodes for high performance asymmetric supercapacitors. *J. Power Sources* **2020**, *465*, No. 228239.

(44) Zhang, G.; Ren, L.; Deng, L.; Wang, J.; Kang, L.; Liu, Z.-H. Graphene-MnO$_2$ nanocomposite for high-performance asymmetrical electrochemical capacitor. *Mater. Res. Bull.* **2014**, *49*, 577−583.